J MATER RES TECHNOL. 2019;8(2):1746–1760

Available online at www.sciencedirect.com

jmr&t Journal of Materials Research and Technology

www.jmrt.com.br

Original Article

An extensive study on the synthesis of iron based magnetic aluminium oxide nanocomposites by solution combustion method

Merve Pehlivan[a], *Sinem Simsek*[a], *Sunullah Ozbek*[b,*], *Belma Ozbek*[a,*]

[a] *Yildiz Technical University, Chemical Engineering Department, Davutpasa Campus, Esenler/Istanbul 34220, Turkey*

[b] *Istanbul Gedik University, Metallurgy and Materials Engineering Department, Kartal Campus, Kartal/Istanbul 34876, Turkey*

ARTICLE INFO

Article history:
Received 13 August 2018
Accepted 7 December 2018
Available online 31 January 2019

Keywords:
Iron based magnetic aluminium oxide nanocomposites
Fuel types
Solution combustion method
Calcination
Reduction
Characterization studies

ABSTRACT

In the present study, it was aimed to investigate the synthesis of iron based magnetic aluminium oxide nanocomposites (IMANCs) by solution combustion (SC) method using various fuel types at various amounts. IMANCs were synthesized using aluminium nitrate and iron nitrate as oxidizers. Urea, glycine and sucrose were chosen as fuel types at various amounts, respectively, to examine their effects on size and morphology of nanocomposites synthesized. The chemical compositions, morphologies and thermal behaviors of IMANCs synthesized were compared with data obtained from characterization studies using X-Ray Diffraction (XRD), Scanning Electron Microscopy (SEM) and Energy Dispersive X-ray Spectroscopy (EDS), Thermogravimetric and Differential Thermal Analysis (TG/DTA), Fourier Transform Infrared Analysis (FT-IR), Surface Area and Porosity Analyzer. The characterization studies revealed that IMANCs were synthesized successfully by SC method with nanoscale properties. It was found that IMANCs synthesized using stoichiometric amount of glycine had porous and smaller particle size with higher surface area compared to other samples synthesized by urea and sucrose, respectively. There is no documentation found on glycine based synthesis of IMANCs by SC method in the literature so far. Additionally, this original paper is the first report on the synthesis of IMANCs by applying calcination and reduction processes following SC reaction using various fuel types at various amounts. It was resulted that the samples synthesized by SC method had smaller particle sizes compared to the samples which were synthesized by applying calcination and reduction processes following SC reaction using stoichiometric amount of urea, glycine and sucrose as fuel types, respectively.

* *Corresponding author.*
E-mails: sunullah.ozbek@gmail.com (S. Ozbek), bozbek@yildiz.edu.tr (B. Ozbek).

https://doi.org/10.1016/j.jmrt.2018.12.005

1. Introduction

Nanoscience has been defined as the key factor for unlocking new generation of materials and art of manipulating matter at the nanoscale [1,2] such as nanoparticles, nanocrystals, nanofibers, nanocomposites, which also overall named as nanostructured materials, with novice properties and functionalities [3–30]. Nanoparticles and nanocomposites have created huge interest due to their novel and significant magnetic, electrical, optical, mechanical and chemical reactivity properties thanks to their small size and high surface area to volume ratio when compared to their bulk materials [31,32]. In the literature, many studies were demonstrated on the synthesis of various nanocomposites/nanoparticles with various methods for their applications in various fields [33–43].

Aluminium oxide, one of the superior nanostructured materials, although has several crystalline structures as stated by [44], alpha phase aluminium oxide (α-Al_2O_3) and gamma phase aluminium oxide (γ-Al_2O_3) are the most known crystalline structures [45]. Even, α-Al_2O_3 and γ-Al_2O_3 contain the same ratio of Al and O atoms, the only difference between them is their crystal structure. α-Al_2O_3 and γ-Al_2O_3 have hexagonal and tetragonal crystal structure, respectively [46]. α-Al_2O_3 is known as the most stable phase of aluminium oxide, and γ-Al_2O_3 is mostly defined as amorphous with porous structure [47]. Aluminium oxide nanoparticles have chemical, electrical, optical, thermal and catalytic properties besides their physico-chemical properties like hardness, improved thermal stability, superior strength to bases and acids, mechanical strength, eminent insulation and transparency properties [32,48,49]. Moreover, relevant nanoparticles are widely studied for advanced engineering applications such as catalyst of reactions, additive of paints, pigments or ceramics, refractory materials, abrasive grains, biocompatible materials, nanocomposite for structural and electrical applications, etc. [32,50,51].

Even though nanoparticles have favored properties, they are subjected to be generated in better and/or customized versions to meet the requirements. By combining two or more materials, it is possible to produce the nanocomposites with synergetic and improved properties [52]. Composite materials based on polymeric, ceramic or metallic matrices reinforced with ferrite nanoparticles can be used as biomedical materials, drug delivery materials, magnetic contrast agents, catalysts, pigments, purifiers and removing substances such as ions, impurities, etc. [53]. It was also studied on the synthesis of iron and iron based magnetic nanoparticles and nanocomposites as those materials provides high saturation magnetization and high coercivity [54–56]. By applying magnetic field, iron based magnetic nanocomposites can be separated from the liquid phase. Hence, magnetic nanocomposites have increasing attention for many application areas such as catalysts, ferrofluids, clinic drug delivery, magnetic storage media, color imaging, effective adsorbents, etc. [52,57–59]. However, the oxidation occurred on the surfaces of the iron particles cause a major problem, that can be solved by embedding iron nanoparticles into aluminium oxide nanoparticles [59].

There are various synthesis methods for preparation of nanoparticles or nanocomposites such as sol–gel method [60], hydrothermal method [61], wet impregnation method [52], high-energy ball milling method [59], co-precipitation [62] and solution combustion method [51], etc. Among these methods, the solution combustion synthesis (SCS) which was firstly used in 1980 for production of nanoscale materials has several advantages. SCS is a self-sustained thermal process including several exothermic reactions. Even, SCS process can be considered as self-propagating high-temperature synthesis (SHS) or combustion synthesis (CS) [63], that has several differences from SHS and CS such as (i) the initial components are mixed in aqueous solution at the molecular level and sizes of ions in the solution are in range from 0.1 to 1 nm at SCS process. Solid powders are used for SHS process and the sizes of powder are in the range from $\sim 10^2$ to 10^5 nm, (ii) for SCS method, the majority heat is generated from oxidation of organic fuel components, but for SHS method, the heat is generated during synthesis reaction, and (iii) SCS method produces large amount of gaseous products during the reaction which enables to provide porous and finely dispersed solid nanoparticles [64].

On the other hand, SCS method depends on chemical composition of oxidizer, fuel and solvent used. For example; metal nitrates, hydrates, sulfates and carbonates are used as oxidizer or reducing agents and urea, sucrose, glucose or other water soluble carbohydrates are used as a fuel type [51,65]. The solution combustion reaction mechanism is effected with respect to flame types, fuel types, fuel to oxidizer ratio, ignition temperature, water amount, etc. [31]. SCS method provides homogeneously distributed, nonagglomerated, multi-component nanopowders for their usage as catalyst, preparation materials for fuel cells, etc. [66]. In addition to being a quick and easy process, SCS has more advantages such as low cost, saving time and energy for synthesis of high purity grade and homogeneous nanosize powders without usage of further thermal treatments compared to other methods [2,31,63]. For example, in co-precipitation method, reactions are hard to control and this feature indicated that is not a repeatable method for synthesize of nanoparticles and nanocomposites [32,50]. Sol–gel method known as a low-cost technique, but this method has some difficulties in controlling of the synthesis and the drying steps, and also accumulation of the contaminants in the gel [32,67,68]. Moreover, high-energy ball milling method provides a wide particle size distributions and residues remaining on the surface due to contamination [32,69].

In the study performed by Wang et al. [65], iron based magnetic aluminium oxide nanocomposites (IMANCs) were synthesized by solution combustion method using urea as fuel type. They stated that the calcination is the necessary step to obtain Fe_2O_3/Al_2O_3 nanocomposites, although the solution combustion reaction was carried out at high temperature. Zhang et al. [70] synthesized Fe_2O_3/Al_2O_3 nanocomposites by solution combustion method. They reported that Fe_2O_3/Al_2O_3 had regular, spheroidal shape and porous structure from SEM and TEM images, and their averagely pore size and surface area were found as 64.76 nm and 4.01 m^2/g, respectively.

Therefore, in the present study, it was aimed to synthesize iron based magnetic aluminium oxide nanocomposites (IMANCs) by solution combustion method using various fuel types at various amounts. For this purpose, urea, glycine

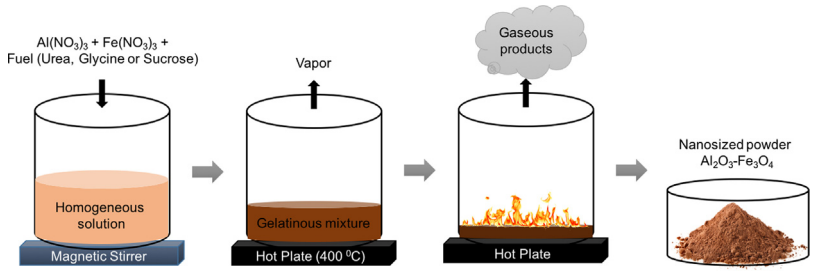

Fig. 1 – Schematic representation of SCS process for IMANCs synthesis.

and sucrose were used as fuel types at various amounts to investigate their effects on the size and morphology of nanocomposites synthesized. There is no report on the solution combustion method for synthesis of iron based magnetic aluminium oxide nanocomposites (IMANCs) using glycine as a fuel has yet been published in the literature. Besides, no report was found on the synthesis of IMANCs by applying the calcination and reduction processes following the solution combustion reaction using various fuel types at various amounts. Then, the characterization studies of IMANCs synthesized were performed by X-Ray Diffraction (XRD), Scanning Electron Microscopy (SEM) and Energy Dispersive X-ray Spectroscopy (EDS), Thermogravimetric and Differential Thermal Analysis (TG/DTA), Fourier Transform Infrared Analysis (FT-IR), and Surface Area and Porosity Analyzer. As a result, IMANCs synthesized can be utilized as a potential nano-adsorbent for adsorption of various substances from aqueous solutions, etc.

2. Materials and methods

Aluminium nitrate nonahydrate ($Al(NO_3)_3{\cdot}9H_2O$), iron nitrate nonahydrate ($Fe(NO_3)_3{\cdot}9H_2O$) and sucrose ($C_{12}H_{22}O_{11}$) were purchased from Merck. Urea (98+ %) ($CO(NH_2)_2$) and glycine (99%) ($C_2H_5NO_2$) were obtained from Alfa Aesar.

2.1. *Preparation of iron based magnetic aluminium oxide nanocomposites*

Iron based magnetic aluminium oxide nanocomposites (IMANCs) were synthesized using two oxidizers, aluminium nitrate $Al(NO_3)_3$ and iron nitrate $Fe(NO_3)_3$, and three fuel types, urea ($CO(NH_2)_2$), glycine ($C_2H_5NO_2$) and sucrose ($C_{12}H_{22}O_{11}$) at various fuel amounts, respectively, by solution combustion method. The schematic representation of SCS process for IMANCs synthesis is represented in Fig. 1.

Firstly, precursor solutions were prepared for the synthesis of relevant nanocomposites. For this purpose, oxidizer solutions were prepared by adding 15 g of $Al(NO_3)_3$ and 15 g of $Fe(NO_3)_3$ to 24 mL of distilled water, respectively, and they were mixed until obtaining homogeneous solution by magnetic stirrer. Similarly, 16.67 M urea, 3.33 M glycine and 2.92 M sucrose homogeneous solutions were prepared to be used as fuel solution. Secondly, 11 mL of $Al(NO_3)_3$ solution was mixed with 11 mL of $Fe(NO_3)_3$ solution, and stirred at 500 rpm by magnetic stirrer without any heating. Then, after adding 3 mL of 16.67 M urea solution (coded as SC-FA-U1), the final mixture was stirred at 500 rpm for 15 min at room temperature. Then, this mixture was heated up to 400 °C on the hot plate without mixing. During heating, a gelatinous mixture was formed due to the evaporation. By the release of gaseous products, the solution combustion reaction suddenly took place and continued until the solution become free from water to form final foam-like product. This step continued approximatively 20 min.

For the rest of the sample preparations, similarly, 6 mL of urea (coded as SC-FA-U2), 9 mL of glycine (coded as SC-FA-G1), 18 mL of glycine (coded as SC-FA-G2), 2.25 mL of sucrose (coded as SC-FA-S1) and 4.5 mL of sucrose solutions (coded as SC-FA-S2) were added respectively to precursor mixture of $Al(NO_3)_3$ and $Fe(NO_3)_3$. SC-FA-U1, SC-FA-G1 and SC-FA-S1 were synthesized using 50% of stoichiometric amount of fuel. On the other hand, SC-FA-U2, SC-FA-G2 and SC-FA-S2 were synthesized using stoichiometric amount of fuel (100%). The oxidizers, fuel types and stoichiometric fuel ratios for synthesis of IMANCs by solution combustion method are given in Table 1 in details.

Table 1 – The oxidizers, fuel types and stoichiometric fuel ratios for iron based magnetic aluminium oxide nanocomposites synthesized by solution combustion method.

Sample name	Oxidizer		Fuel types			Stoichiometric fuel ratio (%)
	$Al(NO_3)_3$ solution (mL)	$Fe(NO_3)_3$ solution (mL)	Urea solution (mL)	Glycine solution (mL)	Sucrose solution (mL)	
SC-FA-U1	11	11	3	–	–	50
SC-FA-U2	11	11	6	–	–	100
SC-FA-G1	11	11	–	9	–	50
SC-FA-G2	11	11	–	18	–	100
SC-FA-S1	11	11	–	–	2.25	50
SC-FA-S2	11	11	–	–	4.5	100

Table 2 – Specifications of synthesized samples.

sample name	Specifications of synthesized samples
SC-FA-U1	Synthesized by 50% of stoichiometric amount of urea as fuel type
SC-FA-U2	Synthesized by stoichiometric amount of urea (100%) as fuel type
SC-FA-U2-H	Synthesized by stoichiometric amount of urea (100%) as fuel type, calcined and then reduced under hydrogen atmosphere
SC-FA-G1	Synthesized by 50% of stoichiometric amount of glycine as fuel type
SC-FA-G2	Synthesized by stoichiometric amount of glycine (100%) as fuel type
SC-FA-G2-H	Synthesized by stoichiometric amount of glycine (100%) as fuel type, calcined and then reduced under hydrogen atmosphere
SC-FA-S1	Synthesized by 50% of stoichiometric amount of sucrose as fuel type
SC-FA-S2	Synthesized by stoichiometric amount of sucrose (100%) as fuel type
SC-FA-S2-H	Synthesized by stoichiometric amount of sucrose (100%) as fuel type, calcined and then reduced under hydrogen atmosphere

During the solution combustion synthesis, the reactions occurred between the oxidizers ($Al(NO_3)_3$ and $Fe(NO_3)_3$) and the fuels (urea and glycine) were expected as follows (Eqs. (1) and (2)):

$$2Al(NO_3)_3{\cdot}9H_2O + 2Fe(NO_3)_3{\cdot}9H_2O + 10CO(NH_2)_2 \rightarrow Al_2O_3 + Fe_2O_3 + 10CO_2 + 56H_2O + 16\,N_2 \quad (1)$$

$$3Al(NO_3)_3{\cdot}9H_2O + 3Fe(NO_3)_3{\cdot}9H_2O + 10\,C_2H_5NO_2 \rightarrow 3/2Al_2O_3 + 3/2Fe_2O_3 + 20CO_2 + 79H_2O + 14N_2 \quad (2)$$

According to the study performed by [51], the reaction occurred between the oxidizers ($Al(NO_3)_3$ and $Fe(NO_3)_3$) and sucrose was given in Eq. (3).

$$2Al(NO_3)_3{\cdot}9H_2O + Fe(NO_3)_3{\cdot}9H_2O + C_{12}H_{22}O_{11} \rightarrow Al_2O_3 + Fe^{+3} + 6CO + 6C + 38H_2O + 9NO_2 + 3e^- \quad (3)$$

The general thermal dissociation equations of $Al(NO_3)_3$ and $Fe(NO_3)_3$ were given in Eq. (4) [71] and Eq. (5) [72], respectively.

$$Al(NO_3)_3 \rightarrow Al_2O_3 + 6NO_2 + 3/2O_2 \quad (4)$$

$$Fe(NO_3)_3 \rightarrow Fe_2O_3 + 6NO_2 + 3/2O_2 \quad (5)$$

After synthesis reaction step, all final foam-like samples obtained were grinded by using mortar and pestle, washed with distilled water for three times and dried in oven at 100 °C for 1 h. Among the synthesized samples represented in Table 1, the samples coded as SC-FA-U2, SC-FA-G2 and SC-FA-S2 were chosen for further treatments such as calcination and reduction process, respectively.

For the calcination process, the samples were calcined in a furnace at 1000 °C for 1 h for removing the rest of impurities. Then, following the calcination process, these samples were subjected to the reduction process. For this purpose, the samples were reduced at 1000 °C in tube furnace under hydrogen atmosphere for 1 h. The samples, SC-FA-U2, SC-FA-G2 and SC-FA-S2 after calcination and reduction processes, were coded as SC-FA-U2-H, SC-FA-G2-H and SC-FA-S2-H. The nominations of the synthesized samples are presented in Table 2.

Magnetic attractions of the synthesized nanocomposites were checked by using commercially available neodymium magnet (NdFeB), and shown in Table 3.

2.2. *Characterization studies*

The synthesized IMANCs were characterized using the following devices. X-Ray Diffraction patterns (XRD) were obtained using a Philips PANalytical X'Pert Pro analyser with $Cu_{k\alpha}$ radiations and scanning angle 2θ ranged between 10° and 90° with 1°/min scanning rate at 45 kV and 40 mA. Field-emission Scanning Electron Microscopy (FE-SEM) images were obtained using a Gemini Leo-SUPRA 35VP by applying carbon coatings. The compositional analysis of samples was investigated by the mapping results obtained from SEM–EDS analysis.

Table 3 – Magnetic attraction of synthesized samples.

Sample name	Magnetic attraction
SC-FA-U1	No attraction
SC-FA-U2	Attracted
SC-FA-U2-H	Attracted
SC-FA-G1	Attracted (low)
SC-FA-G2	Attracted
SC-FA-G2-H	Attracted
SC-FA-S1	No attraction
SC-FA-S2	Attracted (low)
SC-FA-S2-H	Attracted

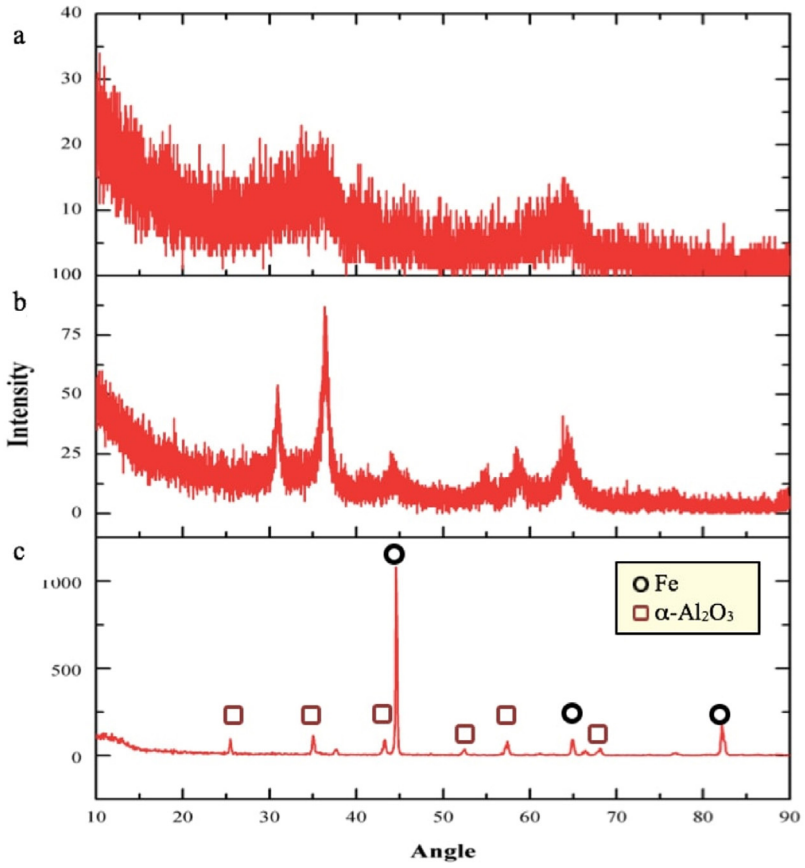

Fig. 2 – XRD patterns of synthesized samples of (a) SC-FA-U1, (b) SC-FA-U2 and (c) SC-FA-U2-H.

Thermogravimetric analysis of the samples was performed using EXSTAR SII TG/DTA6300 from room temperature to 1200 °C with a heating rate of 20 °C/min under air atmosphere. Fourier Transform Infrared (FT-IR) spectroscopy measurements were obtained using a Perkin Elmer Spectrum 100 in the wave number range of 4000–500 cm^{-1}. Samples of FT-IR analysis were prepared by mixing the sample with KBr at a volume ratio of 1:100. BET surface area, pore volume and pore size were examined by analyzing N_2 adsorption/desorption isotherms, using a Quadrasorb SI surface area and pore size analyzer. The surface area of synthesized sample was calculated by Brunauer–Emmett–Teller (BET) theory.

3. Results and discussion

3.1. *X-Ray Diffraction (XRD) analysis*

XRD analyses were carried out for the determination of chemical compositions and identification of phases formed of the synthesized samples. The X-ray diffraction peaks of the samples synthesized using urea as a fuel type coded as SC-FA-U1, SC-FA-U2 and SC-FA-U2-H are shown in Fig. 2a, b and c, respectively. XRD analysis of SC-FA-U1 showed that very low crystallization was developed (Fig. 2a). XRD analysis of SC-FA-U2 suggested that the sample produced is Fe_3O_4 (magnetite) (96-900-2328 entry number) and Al_2O_3 (96-152-8428 entry number) (Fig. 2b). The X-ray diffraction peaks of SC-FA-U2-H are presented in Fig. 2c. The diffraction peaks were displayed at 2θ values of 25.52°, 35.09°, 37.68°, 43.27°, 52.57°, 57.47°, 66.46°, 68.16° and 76.85°. From these peaks, XRD analysis suggested that the sample produced is α-Al_2O_3 (96-900-7497 entry number). Moreover, the diffraction peaks were displayed at 2θ values of 44.61°, 64.93° and 82.25° and the sample produced is iron (Fe) (96-901-3473 entry number).

The X-ray diffraction peaks of the samples synthesized using glycine as a fuel type coded as SC-FA-G1, SC-FA-G2 and SC-FA-G2-H are shown in Fig. 3a, b, and c, respectively. XRD analysis of SC-FA-G1 suggested that the sample produced is Fe_3O_4 (magnetite) (96-900-2327 entry number) and θ-Al_2O_3 (96-120-0006 entry number) (Fig. 3a). XRD analysis of SC-FA-G2 suggested that the sample produced is Fe_3O_4 (magnetite) (96-900-2331 number) and Al_2O_3 (96-810-3515 number). From X-ray patterns of synthesized samples, SC-FA-G1 crystallinity was less than SC-FA-G2 (Fig. 3a and b). The X-ray diffraction peaks of SC-FA-G2-H represented in Fig. 3c were displayed at 2θ values of 25.60°, 35.09°, 37.79°, 43.34°, 52.58°, 57.48°, 66.52° and 66.22°. From these peaks, XRD analysis suggested that the sample produced is α-Al_2O_3 (96-900-7497 entry number). Moreover, the diffraction peaks were displayed at 2θ values of 44.63°, 64.90° and 82.19° and XRD analysis suggested that the sample produced is iron (Fe) (96-901-3473 entry number).

The X-ray diffraction peaks of the samples synthesized using sucrose as a fuel type coded as SC-FA-S1, SC-FA-S2 and SC-FA-S2-H are shown in Fig. 4a, b and c, respectively. The X-ray diffraction peaks of SC-FA-S1 and SC-FA-S2 are presented

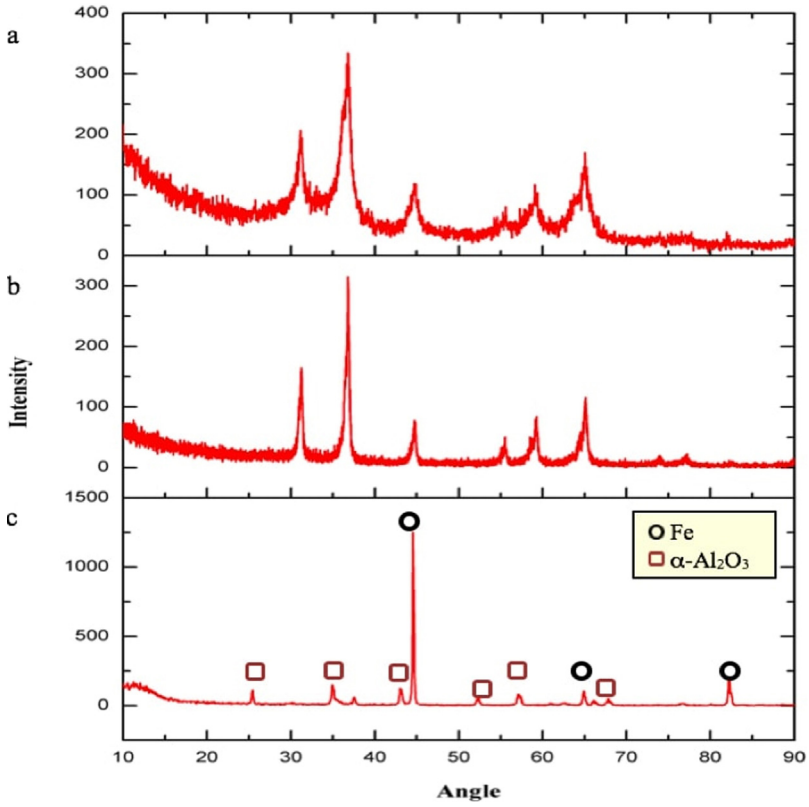

Fig. 3 – XRD patterns of synthesized samples of (a) SC-FA-G1, (b) SC-FA-G2 and (c) SC-FA-G2-H.

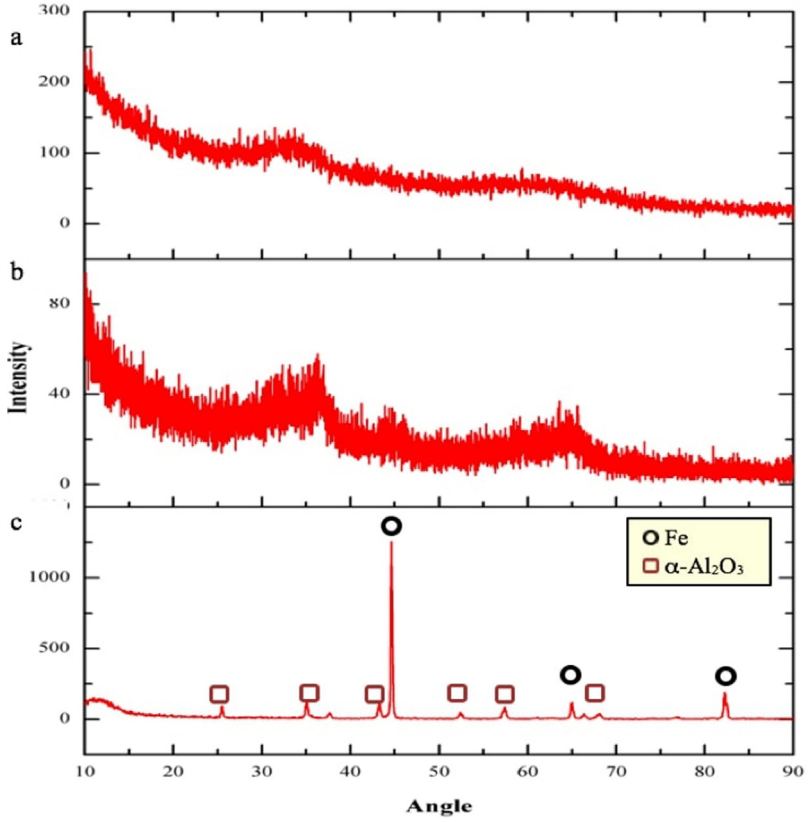

Fig. 4 – XRD patterns of synthesized samples of (a) SC-FA-S1, (b) SC-FA-S2 and (c) SC-FA-S2-H.

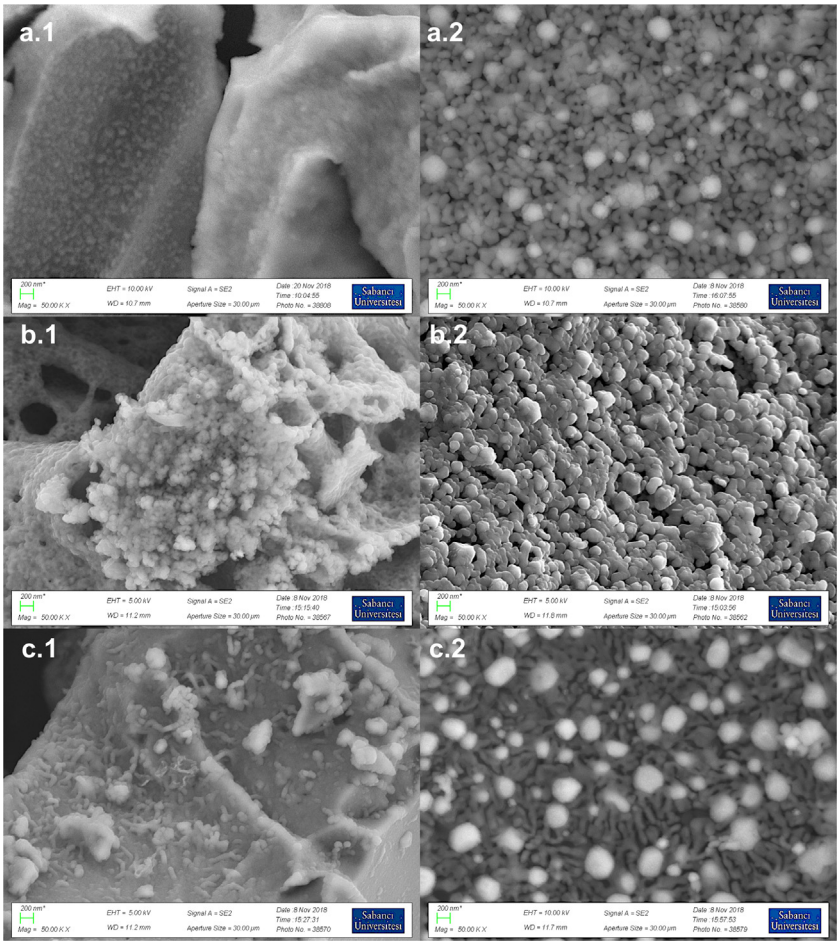

Fig. 5 – SEM images of synthesized samples: (a.1) SC-FA-U2, (a.2) SC-FA-U2-H; (b.1) SC-FA-G2, (b.2) SC-FA-G2-H; (c.1) SC-FA-S2, (c.2) SC-FA-S2-H.

in Fig. 4a and b. XRD analysis suggested that the sample produced seem to be amorphous structure. The X-ray diffraction peaks of SC-FA-S2-H are presented in Fig. 4c. The X-ray patterns of SC-FA-S2-H were similar to SC-FA-U2-H and SC-FA-G2-H. The diffraction peaks at 2θ values of 25.57°, 35.15°, 37.72°, 43.33°, 52.56°, 57.51°, 61.17° and 66.43°. From these peaks, XRD analysis suggested that the sample produced is α-Al_2O_3 (96-900-9784 entry number). Moreover, the diffraction peaks were displayed at 2θ values of 44.75°, 65.10° and 82.39° and the sample produced is iron (Fe) (96-411-3932 entry number).

3.2. *Scanning Electron Microscopy (SEM) and Energy Dispersive X-ray Spectroscopy (EDS) analysis*

The morphology, surface structures and compositional analysis of the samples were analyzed with SEM–EDS micrographs. From SEM images of the samples synthesized using urea as a fuel type coded as SC-FA-U2 (Fig. 5a.1) and SC-FA-U2-H (Fig. 5a.2), it was found that the composites were synthesized successfully in nanoscale by using urea as a fuel. The particle sizes of SC-FA-U2 and SC-FA-U2-H were determined as approximately 60 nm and 200 nm, respectively. Additionally, these particles were featured mostly spherical shape.

From SEM images of the samples synthesized using glycine as a fuel type coded as SC-FA-G2 (Fig. 5b.1) and SC-FA-G2-H (Fig. 5b.2), the particle sizes of these samples were found around 60 nm and 200 nm, respectively. Besides, the sample of SC-FA-G2 contained very small particles as seen in Fig. 5b.1. Moreover, the formation of porous structures and spherical particle shape was observed from the SEM images of the samples synthesized using glycine as a fuel type (Fig. 5b.1 and 5b.2).

From SEM images of the samples synthesized using sucrose as a fuel type coded as SC-FA-S2 (Fig. 5c.1) and SC-FA-S2-H (Fig. 5c.2), average particle sizes of these samples were found approximately 120 nm and 250 nm, respectively. Moreover, the particle morphology of these samples was spherical. It was concluded that using sucrose as a fuel caused formation of the agglomerated particles.

According to SEM images, the samples calcined in furnace and reduced under hydrogen atmosphere after solution combustion reaction coded as SC-FA-U2-H, SC-FA-G2-H and SC-FA-S2-H had more agglomerated and greater particle size compared to samples produced without calcination and reduction processes, SC-FA-U2, SC-FA-G2 and SC-FA-S2.

The compositional analyses of SC-FA-U2-H, SC-FA-G2-H and SC-FA-S2-H samples were determined by Energy Dispersive X-ray Spectroscopy (EDS) analysis (Fig. 6a.1–c.1).

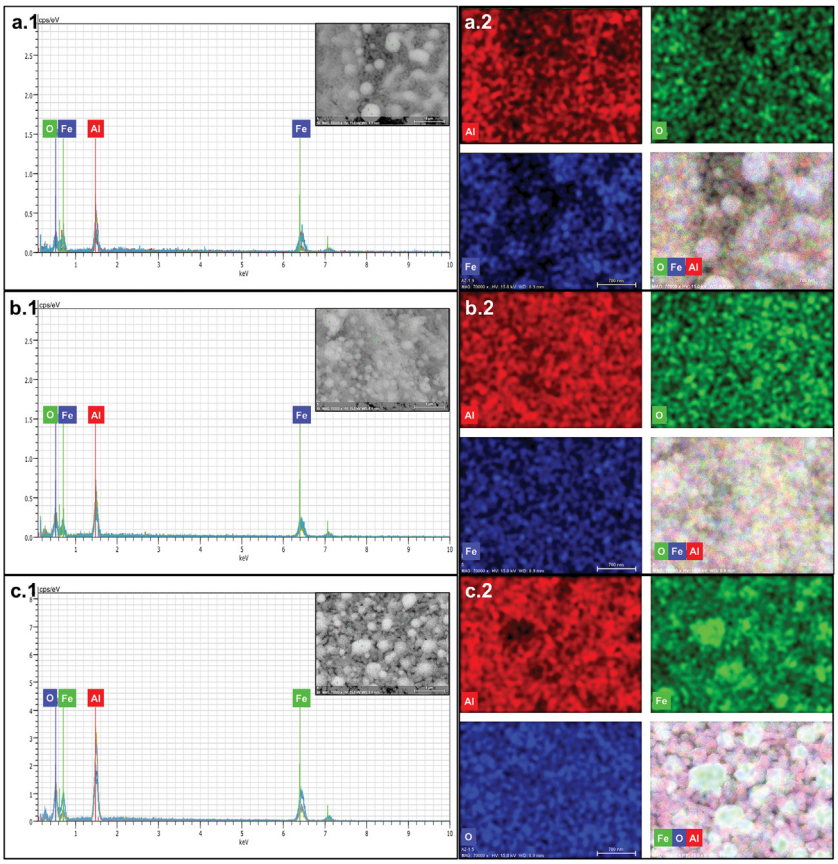

Fig. 6 – SEM–EDS analysis of samples synthesized: SC-FA-U2-H, (a.1) EDS spectrum, (a.2) EDS mapping result; SC-FA-G2-H, (b.1) EDS spectrum, (b.2) EDS mapping result; SC-FA-S2-H, (c.1) EDS spectrum, (c.2) EDS mapping result.

The uniformity of Fe, Al and O atoms distributions were investigated by elemental mapping analysis for SC-FA-U2-H, SC-FA-G2-H and SC-FA-S2-H, as shown in Fig. 6a.2, b.2 and c.2, respectively. The EDS spectrums of the IMANCs were proved the presence of Fe, Al and O atoms within the composites. Consequently, homogenously distributed Fe, Al and O atoms within IMANCs were successfully synthesized.

SC-FA-U2-H, SC-FA-G2-H and SC-FA-S2-H were synthesized to contain 50% by weight of Fe. From EDS analysis, it was obtained that SC-FA-U2-H, SC-FA-G2-H and SC-FA-S2-H were included 59.2, 60.8 and 46.6% weight percentages of Fe, respectively. The compositional analysis of synthesized samples of SC-FA-U2-H, SC-FA-G2-H and SC-FA-S2-H obtained from Energy Dispersive X-ray Spectroscopy (EDS) analysis are given in Table 4.

Table 4 – The compositional analysis of synthesized samples of SC-FA-U2-H, SC-FA-G2-H and SC-FA-S2-H obtained from EDS analysis.

Sample name	Iron (wt%)	Oxygen (wt%)	Aluminium (wt%)
SC-FA-U2-H	59.2	26.5	14.3
SC-FA-G2-H	60.8	25.9	13.3
SC-FA-S2-H	46.6	29.4	24.0

3.3. *Thermogravimetric/Differential Thermal Analysis (TG/DTA)*

The thermal behaviors of the samples before calcination were analyzed by Thermogravimetric and Differential Thermal Analysis (TG/DTA). From TG and DTG curves of SC-FA-U1 (Fig. 7a), initial mass loss of 14.2% from room temperature to 205 °C, corresponding to the evaporation of absorbed water as stated by Maldonado et al. [73]. As can be seen in Fig. 7b, the endothermic reaction took place in the temperature range of room temperature to 205 °C. The second mass loss was observed as 10.4% at the temperature range of 205–700 °C. Lucio-Ortiz et al. [74] suggested that the mass loss could be related to the rest of nitrates and the boehmite transformation into aluminium oxide. As seen in Fig. 7a, very small amount of mass increase was occurred at around 770 °C for sample of SC-FA-U1. This case could be related with the adsorption of oxygen on the particle surface or thermal transformation of iron (III) oxide hydrate as stated by Kalska-Szostko et al. [75] Prasad and Rao [76] explained the thermal transformation of iron (III) oxide hydrate using Eq. (6) as follows:

$$Fe_2O_3{\cdot}2FeOOH{\cdot}2.6H_2O(30–200\,^{\circ}C) \rightarrow 2Fe_2O_3{\cdot}H_2O(220–400\,^{\circ}C) \rightarrow 6Fe_2O_3{\cdot}H_2O(400–450\,^{\circ}C) \rightarrow 6Fe_2O_3{\cdot}H_2O(450–600\,^{\circ}C) \rightarrow \alpha\text{-}Fe_2O_3 \quad (6)$$

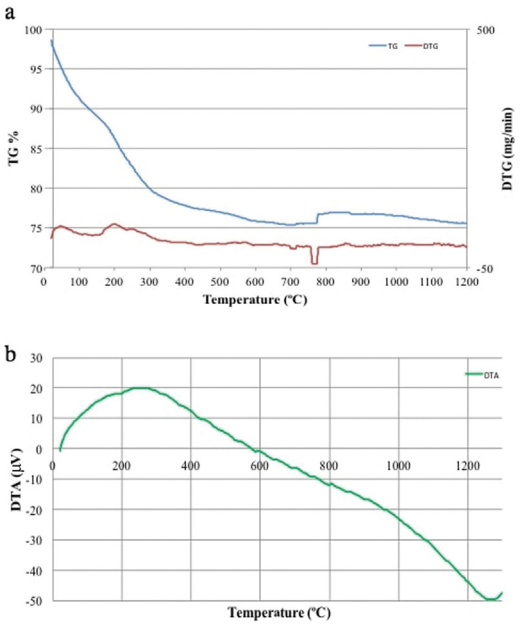

Fig. 7 – (a) TG/DTG curves and (b) DTA curve of SC-FA-U1.

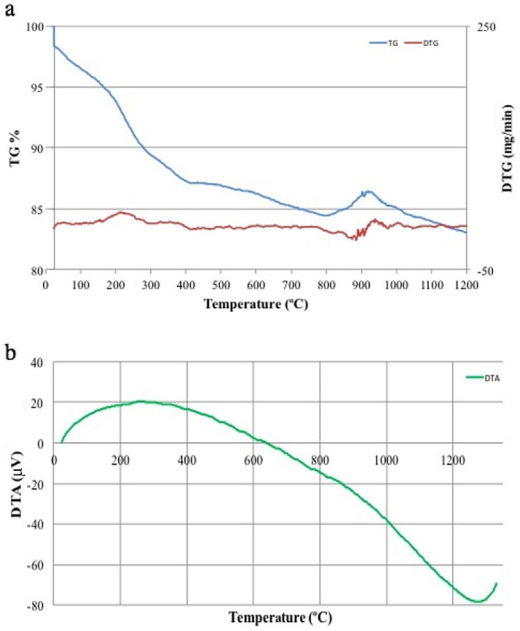

Fig. 8 – (a) TG/DTG curves and (b) DTA curve of SC-FA-U2.

From TG and DTG curves of SC-FA-U2 (Fig. 8a), the initial mass loss of 7% between 25 °C and 215 °C can be attributed to physically absorbed water. From Fig. 8b, the endothermic reaction took place at the temperature range of 25–215 °C. The second mass loss was detected as 5.7% at the temperature range of 215–400 °C due to the decomposition of nitrates, boehmite-aluminium oxide conversion and formation of iron oxide as also stated by Maldonado et al. [73]. A slight increase of mass was observed for SC-FA-U2 sample as seen in Fig. 8a. The reason of the mass gain can be explained by the adsorption of oxygen on the particle surface or thermal transformation of iron (III) oxide hydrate as stated in the studies performed by Kalska-Szostko et al. [75] and Prasad and Rao [76].

From TG and DTG curves of SC-FA-G1 (Fig. 9a), initial mass loss of 10% between 25 °C and 261 °C can be attributed to physically absorbed water. Fig. 9b shows occurrence of the endothermic reaction. The second mass loss was 4% at the temperature range of 261–410 °C, corresponding to the decomposition of nitrates, boehmite aluminium oxide conversion and formation of iron oxide as stated in the study performed by Maldonado et al. [73]. A slight increase of mass was observed for the sample of SC-FA-G1 as seen in Fig. 9a. The cause of the mass gain may be the adsorption of oxygen on the particle surface or phase transformation of iron oxide as stated in the study performed by Kalska-Szostko et al. [75]. Additionally, the color of SC-FA-G1 changed after thermogravimetric analysis.

From TG and DTG curves of SC-FA-G2 (Fig. 10a), the mass loss was 6% between the temperatures of 25 °C and 450 °C, corresponding to evaporation of physically absorbed water (Fig. 10b), boehmite aluminium oxide conversion and formation of iron oxide as mentioned by Maldonado et al. [73] in their

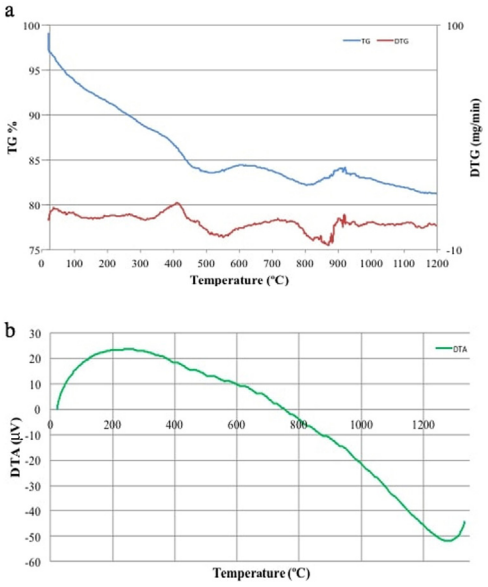

Fig. 9 – (a) TG/DTG curves and (b) DTA curve of SC-FA-G1.

study. From TG curve of SC-FA-G2, a slight increase of mass was observed. The reason of the mass gain can be explained by the adsorption of oxygen on the particle surface or phase transformation of iron oxide as stated by Kalska-Szostko et al. [75] in their study.

From TG and DTG curves of SC-FA-S1 (Fig. 11a), the endothermic reaction was occurred at the temperatures of 25–230 °C (Fig. 11b). In the first region, the temperature range of 25–230 °C, the mass loss was obtained as 11% due to the evaporation of absorbed water. In the second region, at the temperature range of 230–370 °C, 17.3% mass loss was observed. This could be associated with decomposition of nitrates and evaporation of water. In the final region, 4% mass

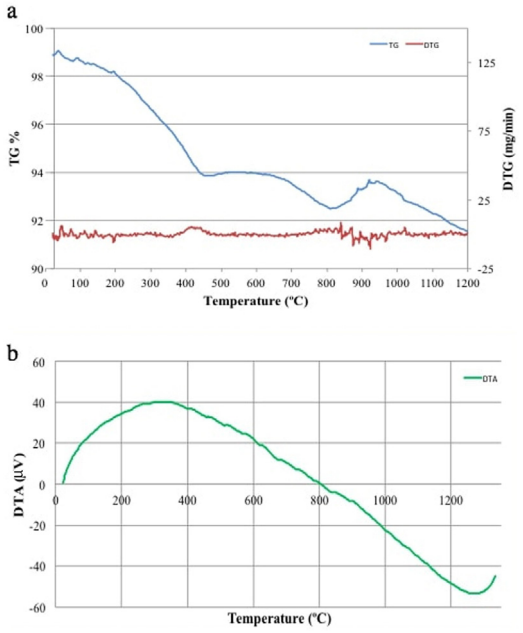

Fig. 10 – (a) TG/DTG curves and (b) DTA curve of SC-FA-G2.

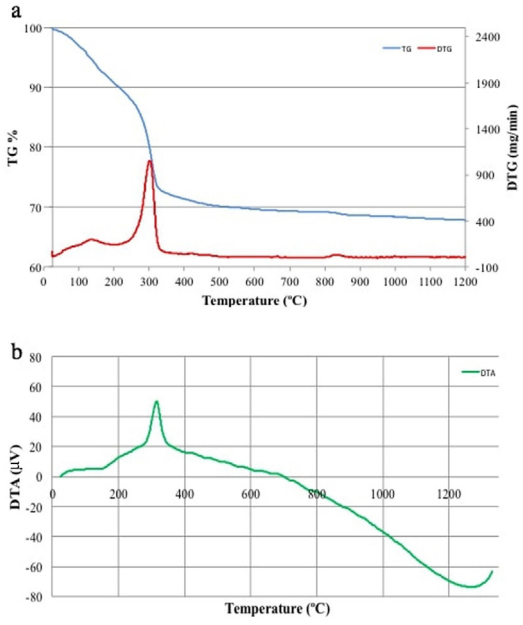

Fig. 11 – (a) TG/DTG curves and (b) DTA curve of SC-FA-S1.

loss was observed, and this could be corresponding to the conversion of boehmite into α-Al_2O_3 and formation of iron oxide as stated by Maldonado et al. [73] and Lucio-Ortiz et al. [74] in their study.

From TG and DTG curves of SC-FA-S2 (Fig. 12a), the significant mass loss was detected in three regions. In the first region, 11% of mass loss occurred at the temperature of between 25 °C and 200 °C, this can be attributed to removal of absorbed water (Fig. 12b). In the second region, 3.5% mass loss was observed at the temperature from 200 °C to 315 °C.

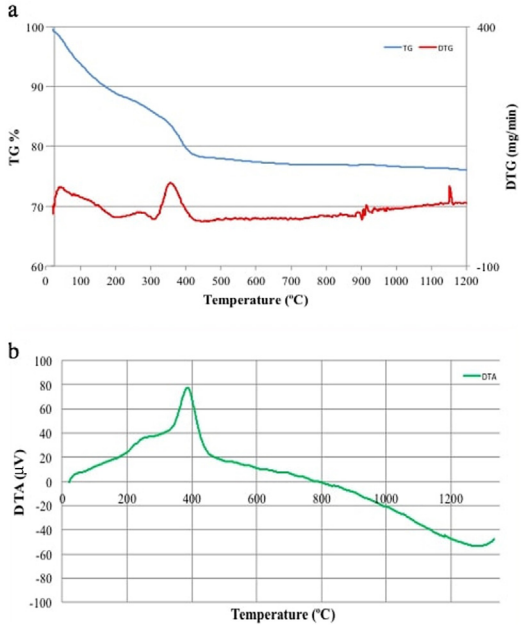

Fig. 12 – (a) TG/DTG curves and (b) DTA curve of SC-FA-S2.

This can be associated with decomposition of nitrates and evaporation of water. In the final region, 7.5% mass loss was observed between 315 °C and 450 °C, corresponding to the conversion of boehmite into α-Al_2O_3 and formation of iron oxide as stated by Maldonado et al. [73] and Lucio-Ortiz et al. [74] in their study.

3.4. *Fourier Transform Infrared (FT-IR) Analysis*

The chemical structures of the synthesized samples were determined by Fourier Transform Infrared (FT-IR) Spectroscopy, and the FT-IR spectra are illustrated in Fig. 13 for all samples examined. Broad O–H stretching band appeared at around 3600–3200 cm^{-1} revealed the presence of hydroxyl groups [77] as supported by TG/DTA analysis shown in Figs. 7–12. The samples synthesized using sucrose as fuel type coded as SC-FA-S1 and SC-FA-S2 showed the medium band at about 2340 cm^{-1} was ascribed to groups CO_2 as stated by Zhang et al. [70] in their study. The additional peaks appeared in the region of 1600–1300 cm^{-1} were mainly ascribed to the bending vibration of ionic CO_3^{-2} [65,70]. The band at 850–580 cm^{-1} was assigned to Al–O vibration in IMANCs as stated by Bozorgpour et al. [77] in their study. Besides, the formation of Fe_3O_4 nanoparticles was confirmed with the peaks laying in the region between 600 cm^{-1} and 500 cm^{-1} were corresponding to Fe_3O_4 as mentioned by Yew et al. [78] in their study. The peaks of synthesized IMANCs were found at about 550 cm^{-1} in the spectra, which is associated with stretching vibration mode of Fe–O [70,77,78]. Besides, as seen in Fig. 13, for the samples of SC-FA-U2-H, SC-FA-G2-H and SC-FA-S2-H, the disappearance of the characteristic bands in the region of 4000–1000 cm^{-1} was observed after the calcination and reduction processes.

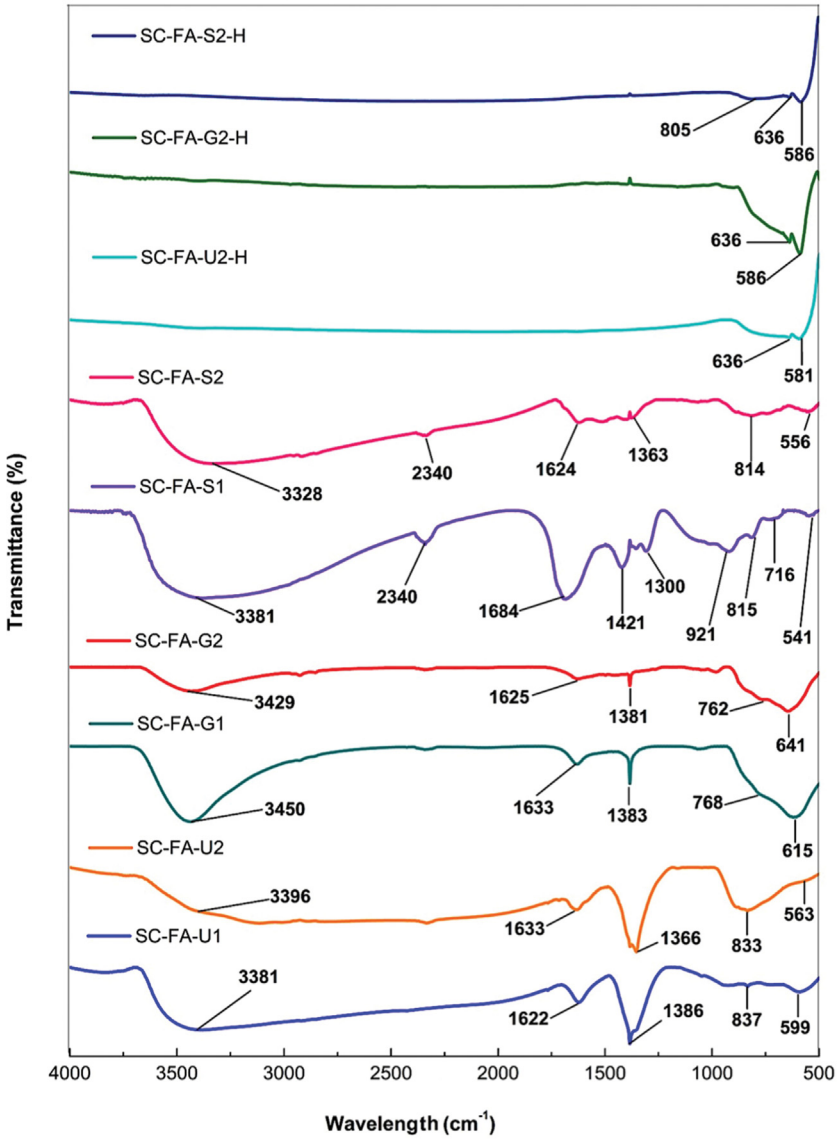

Fig. 13 – FT-IR spectra of samples synthesized.

3.5. *Surface Area and Porosity Analysis*

According to the results obtained from SEM analysis as seen in Fig. 5, the samples of SC-FA-G2 and SC-FA-G2-H among other synthesized samples examined showed more porous structure. Therefore, these two samples were chosen for further analysis of the surface area and porosity. From surface area and porosity analysis, the sample of without calcination and reduction processes coded as SC-FA-G2 (19.69 m^2/g) had approximately 4 times greater surface area than the sample of calcined in furnace and then reduced under hydrogen atmosphere coded as SC-FA-G2-H (4.95 m^2/g) (Table 5). Additionally, Zhang et al. [70] in their study also synthesized iron based aluminium oxide composites (Fe_2O_3/Al_2O_3) by solution combustion method using stoichiometric amount of urea as fuel. They found that the synthesized sample has approximately 4.01 m^2/g surface area which is 5 times less than the surface area of the sample synthesized in the present study. The only difference between two studies is the fuel type used during the synthesis of the samples.

Table 5 – Surface area and porosity analysis of SC-FA-G2 and SC-FA-G2-H.

Parameters	SC-FA-G2	SC-FA-G2-H
S_{BET} (m^2/g)	19.69	4.95
Pore volume$_{(BJH\ adsorption)}$ (cm^3/g)	0.0693	0.0319
Pore volume$_{(BJH\ desorption)}$ (cm^3/g)	0.0719	0.0321
$V_{micropore}$ (cm^3/g)	0.0023	0.0007
Pore size$_{(BJH\ adsorption)}$ (nm)	18.74	41.89
Pore size$_{(BJH\ desorption)}$ (nm)	14.83	35.44

The adsorption–desorption isotherms and pore volume analysis by BJH desorption method of SC-FA-G2 sample are shown in Fig. 14. From IUPAC classifications of

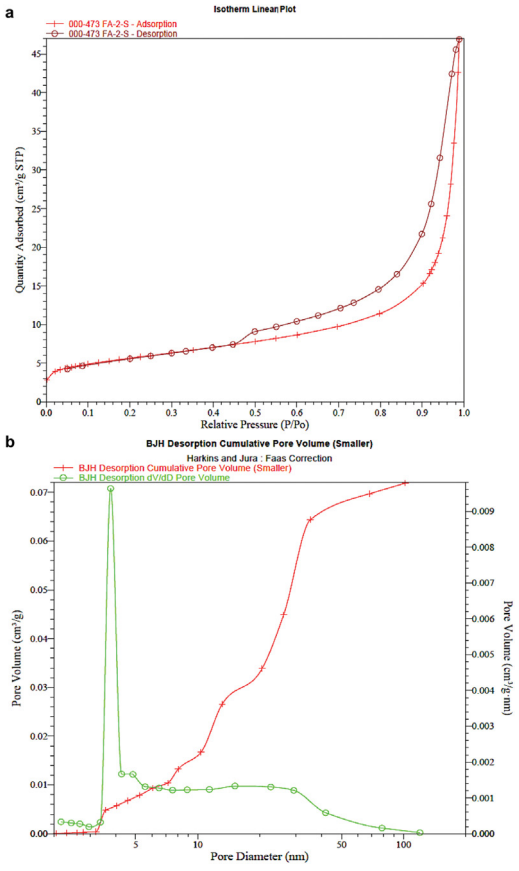

Fig. 14 – (a) The adsorption–desorption isotherms and (b) pore volume analysis by BJH desorption method of SC-FA-G2.

adsorption isotherms, the Type II isotherm was found as the best adsorption–desorption isotherms for SC-FA-G2. Type II isotherm obtained with a non-porous or macroporous adsorbent as stated by Alothman [79]. Moreover, Type II(b) isotherm exhibit Type H3 hysteresis loop. Similar hysteresis loop was also obtained in the present study with SC-FA-G2 in the partial pressure range of 0.45–0.98 (Fig. 14a). The narrow hysteresis loop is the result of inter-particle capillary condensation, usually within a nonrigid aggregate as stated by Rouquerol et al. [80]. From the pore size analysis (Fig. 14b), the pore size values approached to 18.74 nm and 14.83 nm after adsorption and desorption analysis by the BJH method, respectively.

4. Conclusions

In the present study, iron based magnetic aluminium oxide nanocomposites (IMANCs) were synthesized by solution combustion method using $Al(NO_3)_3$ and $Fe(NO_3)_3$ as oxidizers and urea, glycine or sucrose as fuel types at the amounts of stoichiometrically 50% and 100%. The synthesized samples were characterized by XRD, SEM–EDS, TG/DTA, FT-IR and Surface Area and Porosity Analyzer. The main findings were summarized as follows:

- From XRD analysis, SC-FA-U1 showed amorphous character. On the other hand, SC-FA-U2 showed crystalline structure of nanocomposite (Fe_3O_4 and Al_2O_3) formation.
- XRD analysis of SC-FA-G1 and SC-FA-G2 showed the crystalline structure. SC-FA-G1 comprises of Fe_3O_4 and θ-Al_2O_3, whereas SC-FA-G2 comprises of Fe_3O_4 and Al_2O_3.
- From XRD analysis of SC-FA-S1 and SC-FA-S2, developed amorphous structure.
- XRD analysis of SC-FA-U2-H, SC-FA-G2-H and SC-FA-S2-H, showed that all the samples have α-Al_2O_3 and Fe formation. Besides, reduction of iron based magnetic aluminium oxide nanocomposites under hydrogen atmosphere was needed for transformation of Fe_2O_3 to Fe.
- Only the samples of SC-FA-U2, SA-FA-U2-H, SC-FA-G1, SC-FA-G2, SA-FA-G2-H, SA-FA-S2 and SA-FA-S2-H showed the magnetic attraction which were checked by commercially available neodymium magnet (NdFeB).
- From SEM images, the samples of SC-FA-U2, SC-FA-G2 and SC-FA-S2 synthesized by solution combustion method had smaller particle size at around 60 nm, 60 nm and 120 nm, respectively. In contrast with, the samples which were synthesized by applying the calcination and reduction processes following the SC reaction (SC-FA-U2-H, SC-FA-G2-H and SC-FA-S2-H) had particle size at around 200 nm, 200 nm and 250 nm, respectively. Moreover, SC-FA-G2 showed more porous structure among the other synthesized samples.
- The EDS spectrums of the IMANCs were proved the presence of Fe, Al and O atoms within the composites. Besides, the EDS mapping showed that the synthesized IMANCs showed homogeneously distributed structure.
- The results obtained from TG/DTA analyses of synthesized samples were also confirmed by XRD analysis. The mass gain observed for the samples synthesized using urea and glycine as fuel types, and that could be explained by the oxidation of the particles causing an increase.
- FT-IR spectra showed the formation of IMANCs due to vibrations of Al–O and Fe–O according to presence of the absorption peaks in the range of 850–500 cm^{-1}.
- The surface area of SC-FA-G2 synthesized by solution combustion method using stoichiometric amount of glycine was found as 19.69 m^2/g that was five times higher compared to the value obtained, 4.01 m^2/g, in the study performed by Zhang et al. [70].

To sum up, according to the data obtained from the characterization studies, it was concluded that IMANC synthesized by solution combustion method using stoichiometric amount of glycine as fuel type, coded as SC-FA-G2, showed more porous structure and smaller particle size distribution compared to other samples synthesized. Hence, for further studies, the potential usage of SC-FA-G2 sample as an effective nano-adsorbent can be investigated for the adsorption of various substances such as proteins, heavy metals, dyes, drugs, etc. from aqueous solutions on waste water treatment, etc.

Conflicts of interest

The authors declare no conflicts of interest.

Acknowledgements

The present study was carried at both laboratories of Yildiz Technical University, Chemical Engineering Department and İstanbul Gedik University, Metallurgy and Materials Engineering Department. Also, this research has been supported by the Scientific and Technological Research Council of Turkey (TUBITAK), Project No. 315M495. Sinem Simsek gratefully acknowledges the Scientific and Technological Research Council of Turkey (TUBITAK) for the scholarship.

REFERENCES

[1] Sombra dos Santos F, Lago FR, Yokoyama L, Fonseca FV. Synthesis and characterization of zero-valent iron nanoparticles supported on SBA-15. J Mater Res Technol 2017;6:178–83, http://dx.doi.org/10.1016/j.jallcom.2017.07.105.

[2] Jadhav LD, Patil SP, Chavan AU, Jamale AP, Puri VR. Solution combustion synthesis of Cu nanoparticles: a role of oxidant-to-fuel ratio. Micro Nano Lett 2011;6:812–5, http://dx.doi.org/10.1049/mnl.2011.0372.

[3] Du H, Zhao CX, Lin J, Guo J, Wang B, Hu Z, et al. Carbon nanomaterials in direct liquid fuel cells. Chem Rec 2018;18:1365–72, http://dx.doi.org/10.1002/tcr.201800008.

[4] Cheng C, Fan R, Wang Z, Shao Q, Guo X, Xie P, et al. Tunable and weakly negative permittivity in carbon/silicon nitride composites with different carbonizing temperatures. Carbon N Y 2017;125:103–12, http://dx.doi.org/10.1016/j.carbon.2017.09.037.

[5] Wang C, Zhao M, Li J, Yu J, Sun S, Ge S, et al. Silver nanoparticles/graphene oxide decorated carbon fiber synergistic reinforcement in epoxy-based composites. Polymer (Guildf) 2017;131:263–71, http://dx.doi.org/10.1016/j.polymer.2017.10.049.

[6] Zhao J, Wu L, Zhan C, Shao Q, Guo Z. Overview of polymer nanocomposites: computer simulation understanding of physical properties. Polymer (Guildf) 2017;133:272–87, http://dx.doi.org/10.1016/j.polymer.2017.10.035.

[7] Sun K, Xie P, Wang Z, Su T, Shao Q, Ryu J, et al. Flexible polydimethylsiloxane/multi-walled carbon nanotubes membranous metacomposites with negative permittivity. Polymer (Guildf) 2017;125:50–7, http://dx.doi.org/10.1016/j.polymer.2017.07.083.

[8] Cui X, Zhu G, Pan Y, Shao Q, Dong M, Zhang Y, et al. Polydimethylsiloxane-titania nanocomposite coating: fabrication and corrosion resistance. Polymer (Guildf) 2018;138:203–10, http://dx.doi.org/10.1016/j.polymer.2018.01.063.

[9] He Y, Yang S, Liu H, Shao Q, Chen Q, Lu C, et al. Reinforced carbon fiber laminates with oriented carbon nanotube epoxy nanocomposites: magnetic field assisted alignment and cryogenic temperature mechanical properties. J Colloid Interface Sci 2018;517:40–51, http://dx.doi.org/10.1016/j.jcis.2018.01.087.

[10] Wu Z, Gao S, Chen L, Jiang D, Shao Q, Zhang B, et al. Electrically insulated epoxy nanocomposites reinforced with synergistic core–shell SiO 2@MWCNTs and montmorillonite bifillers. Macromol Chem Phys 2017;218:1–9, http://dx.doi.org/10.1002/macp.201700357.

[11] Gu H, Zhang H, Lin J, Shao Q, Young DP, Sun L, et al. Large negative giant magnetoresistance at room temperature and electrical transport in cobalt ferrite-polyaniline nanocomposites. Polymer (Guildf) 2018;143:324–30, http://dx.doi.org/10.1016/j.polymer.2018.04.008.

[12] Zhang Y, Zhao M, Zhang J, Shao Q, Li J, Li H, et al. Excellent corrosion protection performance of epoxy composite coatings filled with silane functionalized silicon nitride. J Polym Res 2018;25:1–13.

[13] Lu Y, Biswas MC, Guo Z, Jeon JW, Wujcik EK. Recent developments in bio-monitoring via advanced polymer nanocomposite-based wearable strain sensors. Biosens Bioelectron 2018:1–11, http://dx.doi.org/10.1016/j.bios.2018.08.037.

[14] Gu J, Li Y, Liang C, Tang Y, Tang L, Zhang Y, et al. Synchronously improved dielectric and mechanical properties of wave-transparent laminated composites combined with outstanding thermal stability by incorporating iysozyme/POSS functionalized PBO fibers. J Mater Chem C 2018;6:7652–60, http://dx.doi.org/10.1039/c8tc02391c.

[15] Wang C, Murugadoss V, Kong J, He Z, Mai X, Shao Q, et al. Overview of carbon nanostructures and nanocomposites for electromagnetic wave shielding. Carbon N Y 2018;140:696–733, 10.1016/j.carbon.2018.09.006.

[16] Luo F, Liu X, Yan C, Liu H, Dong M, Mai X, et al. Molecular orientation dependent dynamic viscoelasticity in uni-axially drawn polycarbonate. Polym Test 2018;69:528–35, http://dx.doi.org/10.1016/j.polymertesting.2018.06.009.

[17] Wu Z, Cui H, Chen L, Jiang D, Weng L, Ma Y, et al. Interfacially reinforced unsaturated polyester carbon fiber composites with a vinyl ester-carbon nanotubes sizing agent. Compos Sci Technol 2018;164:195–203, http://dx.doi.org/10.1016/j.compscitech.2018.05.051.

[18] Song B, Wang T, Sun H, Liu H, Mai X, Wang X, et al. Graphitic carbon nitride (g-C_3N_4) interfacially strengthened carbon fiber epoxy composites. Compos Sci Technol 2018;167:515–21, http://dx.doi.org/10.1016/j.compscitech.2018.08.031.

[19] Liu H, Dong M, Huang W, Gao J, Dai K, Guo J, et al. Lightweight conductive graphene/thermoplastic polyurethane foams with ultrahigh compressibility for piezoresistive sensing. J Mater Chem C 2017;5:73–83, http://dx.doi.org/10.1039/c6tc03713e.

[20] Zhao ZY, Guan RG, Zhang JH, Zhao ZY, Bai PK. Effects of process parameters of semisolid stirring on microstructure of Mg–3Sn–1Mn–3SiC (wt%) strip processed by rheo-rolling. Acta Metall Sin (Engl Lett) 2017;30:66–72, http://dx.doi.org/10.1007/s40195-016-0509-8.

[21] Wu N, Liu C, Xu D, Liu J, Liu W, Shao Q, et al. Enhanced electromagnetic wave absorption of three-dimensional porous Fe_3O_4/C composite flowers. ACS Sustain Chem Eng 2018;6:12471–80, http://dx.doi.org/10.1021/acssuschemeng.8b03097.

[22] Guo J, Song H, Liu H, Luo C, Ren Y, Ding T, et al. Polypyrrole-interface-functionalized nano-magnetite epoxy nanocomposites as electromagnetic wave absorbers with enhanced flame retardancy. J Mater Chem C 2017;5:5334–44, http://dx.doi.org/10.1039/c7tc01502j.

[23] Zhao Z, Bai P, Guan R, Murugadoss V, Liu H, Wang X, et al. Microstructural evolution and mechanical strengthening mechanism of Mg–3Sn–1Mn–1La alloy after heat treatments. Mater Sci Eng A 2018;734:200–9, http://dx.doi.org/10.1016/j.msea.2018.07.083.

[24] Sun Z, Zhang L, Dang F, Liu Y, Fei Z, Shao Q, et al. Experimental and simulation-based understanding of morphology controlled barium titanate nanoparticles under co-adsorption of surfactants. CrystEngComm 2017;19:3288–98, http://dx.doi.org/10.1039/c7ce00279c.

[25] Zhang L, Yu W, Han C, Guo J, Zhang Q, Xie H, et al. Large scaled synthesis of heterostructured electrospun TiO_2/SnO_2 nanofibers with an enhanced photocatalytic activity. J Electrochem Soc 2017;164:H651–6, http://dx.doi.org/10.1149/2.1531709jes.

[26] Zhang L, Qin M, Yu W, Zhang Q, Xie H, Sun Z, et al. Heterostructured TiO_2/WO_3 nanocomposites for photocatalytic degradation of toluene under visible light. J Electrochem Soc 2017;164:H1086–90, http://dx.doi.org/10.1149/2.0881714jes.
[27] Zhang Y, Qian L, Zhao W, Li X, Huang X, Mai X, et al. Highly efficient Fe–N–C nanoparticles modified porous graphene composites for oxygen reduction reaction. J Electrochem Soc 2018;165:H510–6, http://dx.doi.org/10.1149/2.0991809jes.
[28] Song B, Wang T, Sun H, Shao Q, Zhao J, Song K, et al. Two-step hydrothermally synthesized carbon nanodots/WO_3 photocatalysts with enhanced photocatalytic performance. Dalton Trans 2017;46:15769–77, http://dx.doi.org/10.1039/c7dt03003g.
[29] Lin C, Hu L, Cheng C, Sun K, Guo X, Shao Q, et al. Nano-$TiNb_2O_7$/carbon nanotubes composite anode for enhanced lithium-ion storage. Electrochim Acta 2018;260:65–72, http://dx.doi.org/10.1016/j.electacta.2017.11.051.
[30] Li Y, Jing T, Xu G, Tian J, Dong M, Shao Q, et al. 3-D magnetic graphene oxide-magnetite poly (vinyl alcohol) nanocomposite substrates for immobilizing enzyme. Polymer (Guildf) 2018;149:13–22, http://dx.doi.org/10.1016/j.polymer.2018.06.046.
[31] Alves AK, Bergmann CP, Berutti FA. Novel synthesis and characterization of nanostructured materials. Eng Mater 2013:11–21, http://dx.doi.org/10.1007/978-3-642-41275-2.
[32] Manivasakan P. Synthesis of Al_2O_3, ZrO_2 and TiO_2 nanoparticles from natural minerals for industrial applications. Anna University of Technology Coimbatore; 2011.
[33] Ghiyasiyan-Arani M, Masjedi-Arani M, Salavati-Niasari M. Simple precipitation synthesis of pure $Cu_3V_2O_8$ nanoparticles and investigation of their optical properties. J Nanostruct 2015;5:437–41.
[34] Monsef R, Ghiyasiyan-Arani M, Salavati-Niasari M. Application of ultrasound-aided method for the synthesis of $NdVO_4$ nano-photocatalyst and investigation of eliminate dye in contaminant water. Ultrason Sonochem 2018;42:201–11, http://dx.doi.org/10.1016/j.ultsonch.2017.11.025.
[35] Perumbilavil S, Sridharan K, Abraham AR, Janardhanan HP, Kalarikkal N, Philip R. Nonlinear transmittance and optical power limiting in magnesium ferrite nanoparticles: effects of laser pulsewidth and particle size. RSC Adv 2016;6:106754–61, http://dx.doi.org/10.1039/c6ra15788b.
[36] Salehabadi A, Salavati-Niasari M, Ghiyasiyan-Arani M. Self-assembly of hydrogen storage materials based multi-walled carbon nanotubes (MWCNTs) and $Dy_3Fe_5O_{12}$ (DFO) nanoparticles. J Alloys Compd 2018;745:789–97, http://dx.doi.org/10.1016/j.jallcom.2018.02.242.
[37] Ghiyasiyan-Arani M, Salavati-Niasari M. Effect of $Li_2CoMn_3O_8$ nanostructures synthesized by a combustion method on montmorillonite K10 as a potential hydrogen storage material. J Phys Chem C 2018;122:16498–509, http://dx.doi.org/10.1021/acs.jpcc.8b02617.
[38] Ghanbari D, Salavati-Niasari M, Ghasemi-Kooch M. A sonochemical method for synthesis of Fe_3O_4 nanoparticles and thermal stable PVA-based magnetic nanocomposite. J Ind Eng Chem 2014;20:3970–4, http://dx.doi.org/10.1016/j.jiec.2013.12.098.
[39] Ghanbari D, Salavati-Niasari M. Synthesis of urchin-like CdS–Fe_3O_4 nanocomposite and its application in flame retardancy of magnetic cellulose acetate. J Ind Eng Chem 2015;24:284–92, http://dx.doi.org/10.1016/j.jiec.2014.09.043.
[40] Ansari F, Bazarganipour M, Salavati-Niasari M. $NiTiO_3/NiFe_2O_4$ nanocomposites: simple sol–gel auto-combustion synthesis and characterization by utilizing onion extract as a novel fuel and green capping agent. Mater Sci Semicond Process 2016;43:34–40, http://dx.doi.org/10.1016/j.mssp.2015.11.014.
[41] Nabiyouni G, Sharifi S, Ghanbari D, Salavati-Niasari M. Coprecipitation synthesis of $CoFe_2O_4$ nanoparticles. J Nanostruct 2014;4:317–23, http://dx.doi.org/10.22059/JUFGNSM.2017.02.04.
[42] Ansari F, Sobhani A, Salavati-Niasari M. Simple sol–gel synthesis and characterization of new $CoTiO_3/CoFe_2O_4$ nanocomposite by using liquid glucose, maltose and starch as fuel, capping and reducing agents. J Colloid Interface Sci 2018;514:723–32, http://dx.doi.org/10.1016/j.jcis.2017.12.083.
[43] Abraham AR, Raneesh B, Woldu T, Aškrabić S, Lazović S, Dohčević-Mitrović Z, et al. Realization of enhanced magnetoelectric coupling and raman spectroscopic signatures in 0–0 type hybrid multiferroic core–shell geometric nanostructures. J Phys Chem C 2017;121:4352–62, http://dx.doi.org/10.1021/acs.jpcc.6b12461.
[44] Wefers K, Misra C. Oxides and hydroxides of aluminum, vol. 19; 1987.
[45] Aswad MA. Residual stress and fracture in high temperature ceramics. The University of Manchester; 2012.
[46] Dey S. Synthesis and application of γ-alumina nanopowders; 2016.
[47] Kamboj NK. The template-assisted wet-combustion synthesis of mesoporous core–shell structured materials. Tallinn University of Technology Faculty; 2016.
[48] Piriyawong V, Thongpool V, Asanithi P, Limsuwan P. Preparation and characterization of alumina nanoparticles in deionized water using laser ablation technique. J Nanomater 2012:1–6, http://dx.doi.org/10.1155/2012/819403.
[49] Zhang D, Nastac L. Numerical modeling of the dispersion of ceramic nanoparticles during ultrasonic processing of aluminum-based nanocomposites. J Mater Res Technol 2014;3:296–302.
[50] Banerjee S. Alumina nanoparticles and alumina-based adsorbents for wastewater treatment. Nanomater Wastewater Remediat 2016:239–72, http://dx.doi.org/10.1016/B978-0-12-804609-8/00010-8.
[51] Kakooei S, Rouhi J, Dehzangi A, Mohammadpour E, Alimanesh M. Synthesis and characterization of Al_2O_3:Fe nanoparticles prepared via aqueous combustion. Casp J Appl Sci Res 2012;1:1–7.
[52] Karakassides MA, Gournis D, Bourlinos AB, Trikalitis PN, Bakas T. Magnetic Fe_2O_3–Al_2O_3 composites prepared by a modified wet impregnation method. J Mater Chem 2003;13:871–6, http://dx.doi.org/10.1039/b211330a.
[53] Dos Santos Aguilera L, Marçal RLSB, De Campos JB, Da Silva MHP, Da Silva Figueiredo ABH. Magnetic filter produced by $ZnFe_2O_4$ nanoparticles using freeze casting. J Mater Res Technol 2018;7:350–5, http://dx.doi.org/10.1016/j.jmrt.2018.04.012.
[54] Ohnuma S, Kobayashi N, Masumoto T, Mitani S, Fujimori H. Magnetostriction and soft magnetic properties of $(Co_{1-x}Fe_x)$–Al–O granular films with high electrical resistivity. J Appl Phys 1999;85:4574–6, http://dx.doi.org/10.1063/1.370412.
[55] Ikeda K, Kobayashi K, Fujimoto M. Multilayer nanogranular magnetic thin films for GHz applications. J Appl Phys 2002;92:5395–400, http://dx.doi.org/10.1063/1.1510562.
[56] Vovk AY, Wang JQ, Pogoriliy AM, Shypil OV, Kravets AF. Magneto-transport properties of CoFe–Al_2O_3 granular films in the vicinity of the percolation threshold. J Magn Magn Mater 2002;242–245:476–8, http://dx.doi.org/10.1016/S0304-8853(01)01061-7.
[57] Munoz M, Pedro ZM De, Menendez N, Casas JA, Rodriguez JJ. A ferromagnetic y-alumina-supported iron catalyst for

CWPO. Application to chlorophenols. Appl Catal B: Environ 2013;136–137:218–24, http://dx.doi.org/10.1016/j.apcatb.2013.02.002.
[58] Liu W, Zhong W, Jiang H, Tang N, Wu X, Du Y. Highly stable alumina-coated iron nanocomposites synthesized by wet chemistry method. Surf Coatings Technol 2006;200:5170–4, http://dx.doi.org/10.1016/j.surfcoat.2005.04.039.
[59] Huang YL, Xue DS, Zhou PH, Ma Y, Li FS. a-Fe-Al_2O_3 nanocomposites prepared by sol–gel method. Mater Eng A 2003;359:332–7, http://dx.doi.org/10.1016/S0921-5093(03)00374-5.
[60] Ahmad I, Siddiqui WA, Qadir S, Ahmad T. Synthesis and characterization of molecular imprinted nanomaterials for the removal of heavy metals from water. J Mater Res Technol 2018;7:270–82, http://dx.doi.org/10.1016/j.jmrt.2017.04.010.
[61] Pattanayak BC. Synthesis and characterization of alumina/iron oxide mixed nanocomposite. National Institue of Technology; 2010.
[62] Reshetenko TV, Avdeeva LB, Khassin AA, Kustova GN, Ushakov VA, Moroz EM, et al. Coprecipitated iron-containing catalysts Fe-methane decomposition at moderate temperatures. I. Genesis of calcined and reduced catalysts. Appl Catal A: Gen 2004;268:127–38, http://dx.doi.org/10.1016/j.apcata.2004.03.045.
[63] Zohourvahid-Karimi E, Moloodi A, Khaki JV. A study on carbon nanotubes/nanofibers production via SHS method in C–Al–Fe_2O_3 system. J Mater Res Technol 2018;7:212–7, http://dx.doi.org/10.1016/j.jmrt.2017.06.005.
[64] Varma A, Mukasyan AS, Rogachev AS, Manukyan KV. Solution combustion synthesis of nanoscale materials. Chem Rev 2016;116:14493–586, http://dx.doi.org/10.1021/acs.chemrev.6b00279.
[65] Wang B, Yan R, Lee DH, Zheng Y, Zhao H, Zheng C. Characterization and evaluation of Fe_2O_3/Al_2O_3 oxygen carrier prepared by sol–gel combustion synthesis. J Anal Appl Pyrolysis 2011;91:105–13, http://dx.doi.org/10.1016/j.jaap.2011.01.010.
[66] Mukasyan AS, Dinka P. Novel approaches to solution-combustion synthesis of nanomaterials. Int J Self-Propag High-Temp Synth 2007;16:23–35, http://dx.doi.org/10.3103/S1061386207010049.
[67] Raab C, Simko M, Fiedeler U, Nentwich M, Gazso A. Production of nanoparticles and nanomaterials. NanoTrust-Doss 2011;6:1–4, http://dx.doi.org/10.1553/ITA-nt-006en.
[68] Shokati Poursani A, Nilchi A, Hassani AH, Shariat M, Nouri J. A novel method for synthesis of nano-γ-Al_2O_3: study of adsorption behavior of chromium, nickel, cadmium and lead ions. Int J Environ Sci Technol 2015;12:2003–14, http://dx.doi.org/10.1007/s13762-014-0740-7.
[69] Muñoz JE, Cervantes J, Esparza R, Rosas G. Iron nanoparticles produced by high-energy ball milling. J Nanopart Res 2007;9:945–50, http://dx.doi.org/10.1007/s11051-007-9226-6.
[70] Zhang J, Guo Q, Liu Y, Cheng Y. Preparation and characterization of Fe_2O_3/Al_2O_3 using the solution combustion approach for chemical looping combustion. Ind Eng Chem Res 2012;51:12773–81.
[71] Sharma A, Rani A, Singh A, Modi OP, Gupta GK. Synthesis of alumina powder by the urea–glycine–nitrate combustion process: a mixed fuel approach to nanoscale metal oxides. Appl Nanosci 2014;4:315–23, http://dx.doi.org/10.1007/s13204-013-0199-8.
[72] Wieczorek-Ciurowa K, Kozak AJ. The thermal decomposition of $Fe(NO_3)_3 \cdot 9H_2O$. J Therm Anal Calorim 1999;58:647–51.
[73] Maldonado CS, De la Rosa JR, Lucio-Ortiz CJ, Hernandez-Ramirez A, Barazza FFC, Valente JS. Low concentration Fe-doped alumina catalysts using sol–gel and impregnation methods: the synthesis, characterization and catalytic performance during the combustion of trichloroethylene. Materials (Basel) 2014;7:2062–86, http://dx.doi.org/10.3390/ma7032062.
[74] Lucio-Ortiz CJ, De la Rosa JR, Ramirez AH, Heredia JADR, Angel PD, Munoz-Aguirre S, et al. Synthesis and characterization of Fe doped mesoporous Al_2O_3 by sol–gel method and its use in trichloroethylene combustion. J Sol-Gel Sci Technol 2011;58:374–84, http://dx.doi.org/10.1007/s10971-011-2403-1.
[75] Kalska-Szostko B, Wykowska U, Satula D, Nordblad P. Thermal treatment of magnetite nanoparticles. Beilstein J Nanotechnol 2015;6:1385–96, http://dx.doi.org/10.3762/bjnano.6.143.
[76] Prasad SVS, Sitakara Rao V. Thermal transformation of iron (III) oxide hydrate gel. J Mater Sci 1984;19:3266–70, http://dx.doi.org/10.1007/BF00549813.
[77] Bozorgpour F, Ramandi HF, Jafari P, Samadi S, Yazd SS, Aliabadi M. Removal of nitrate and phosphate using chitosan/Al_2O_3/Fe_3O_4 composite nanofibrous adsorbent: comparison with chitosan/Al_2O_3/Fe_3O_4 beads. Int J Biol Macromol 2016;93:557–65, http://dx.doi.org/10.1016/j.ijbiomac.2016.09.015.
[78] Yew YP, Shameli K, Miyake M, Kuwano N, Bt Ahmad Khairudin NB, Bt Mohamad SE, et al. Green synthesis of magnetite (Fe_3O_4) nanoparticles using seaweed (*Kappaphycus alvarezii*) extract. Nanoscale Res Lett 2016;11:1–7, http://dx.doi.org/10.1186/s11671-016-1498-2.
[79] Alothman ZA. A review: fundamental aspects of silicate mesoporous materials. Materials (Basel) 2012;5:2874–902, http://dx.doi.org/10.3390/ma5122874.
[80] Rouquerol F, Rouquerol J, Sing KSW, Maurin G, Llewellyn P. Introduction. Adsorpt. by powders porous solids princ. methodol. appl. 2nd ed; 2014. p. 1–24, http://dx.doi.org/10.1016/B978-0-08-097035-6.00001-2.